



# Thermo-hydro-mechanical-chemical (THMC) coupling fracture criterion of brittle rock

Wei YI, Qiu-hua RAO, Zhuo LI, Dong-liang SUN, Qing-qing SHEN

School of Civil Engineering, Central South University, Changsha 410075, China

Received 2 December 2020; accepted 18 May 2021

**Abstract:** Based on analysis of thermo-hydro-mechanical-chemical (THMC) coupling mechanism for brittle rock, THMC coupling indicator in terms of rock porosity was introduced to represent the influencing degree of THMC coupling field on stress field in order to establish THMC coupling fracture criterion. A novel real-time measurement method of permeability (related to porosity) was proposed to determine the THMC coupling indicator, and self-designed THMC coupling tests and scanning electron microscope tests were conducted on pre-cracked red sandstone specimens to study the macroscopic and microscopic fracture mechanism. Research results show that the higher the hydraulic pressure is, the smaller the crack initiation load is and the easier the Mode I fracture occurs. Test results are in good agreement with prediction results (crack initiation load and angle, and fracture mode), which can verify the effectiveness of the newly established THMC coupling fracture criterion. This new fracture criterion can be also further extended to predict THMC coupling fracture of multi-crack problem.

**Key words:** THMC coupling; fracture criterion; THMC coupling indicator; brittle rock

## 1 Introduction

Rock mass is usually subjected to the coupled effect of thermo-hydro-mechanical-chemical (THMC) fields in deep rock mass engineering, such as mineral and petroleum extraction, geothermal utilization and nuclear waste disposal [1–5]. Under the action of these external loadings, natural discontinuous cracks or joints would initiate to result in unstable crack propagation quickly, and ultimate failure of rock mass, especially for brittle rock [6–8]. And thus, it is of great importance to predict the crack initiation (including crack initiation load and angle and fracture mode) for safety assessment and disaster control in deep rock mass engineering.

Currently, there mainly exist two methods for studying crack initiation, namely, experimental and theoretical methods. Many experimental studies

were carried out on cracking behavior of pre-cracked rock specimens under simple and complex loading conditions. For example, WONG and EINSTEIN [9] and YANG and JING [10] conducted uniaxial compression test to investigate crack initiation and propagation process of rock and rock-like specimens with a crack and found that cracking types depend mainly on their geometrical shape and fracture characteristics. YANG [11] adopted uniaxial and triaxial compression tests to check the influence of different temperatures on deformation and fracture coalescence behavior of pre-cracked rock specimen. FENG et al [12,13] and LU et al [14] studied crack initiation and propagation path of fractured rock under HMC coupling condition. They found that the original crack initiates and then propagates along the direction of the uniaxial stress and the effect of chemical solution is largely dependent on its pH value and ionic concentrations. LI et al [15,16] used

tri-axial compression tests to investigate the influence of temperature, hydraulic and confining pressures on fracture trajectory of pre-cracked specimen and found that lower temperature and higher confining pressure benefit to transverse (Mode II) fracture. However, most of previous experimental methods are focused on the investigations of crack initiation and propagation behaviors for brittle rock or rock-like materials under simple and less than or equal to three-field coupling condition, and very few experimental studies were conducted for rock materials under four-field (i.e., THMC) coupling case. Furthermore, although in experimental method we can visually observe crack evolution process under complex loading conditions, there might be difficulty in exactly obtaining stress state of specimen and predicting crack initiation load and angle, and fracture mode [17,18]. In contrast, theoretical method has the advantage of obtaining stress and strain solutions with high accuracy and predicting crack initiation parameters, and thus theoretical method has attracted interests of more and more researchers. In the last several decades, different fracture criteria were presented to study crack initiation. According to various parameters (stress, strain and energy), these criteria can be divided into the following three groups [19]: (1) stress-based fracture criterion, e.g., maximum tensile stress criteria ( $\sigma_0$ -criterion) [20] and maximum tangential principle stress criterion ( $\sigma_{1\theta}$ -criterion) [21]; (2) strain-based fracture criterion, e.g., maximum tangential strain criterion ( $\varepsilon_0$ -criterion) [22]; (3) energy-based fracture criterion, e.g., maximum energy release rate criterion (G-criterion) [23], minimum strain energy density criterion (S-criterion) [24] and maximum volumetric strain energy density criterion (T-criterion) [25,26]. A few researchers also developed these fracture criteria to solve multi-field coupling fracture problem. For example, LI et al [27] established HM coupling energy-based fracture criterion by supposing pre-cracked rock as continuous rock with damage; TAN and WANG [28] developed a new HMC coupling stress-based fracture criterion by taking into account of the influence of water-chemical solution on effective crack length and stress field. Although these fracture criteria can successfully predict Mode I (tensile) fracture for brittle materials under mix-mode and multi-field coupling

conditions, there might be limitations on the true Mode (shear) II fracture [29,30]. This is because the tensile strength of brittle rock is usually smaller than its shear strength, and Mode I fracture easily occurs before Mode II fracture. A new fracture criterion based on the ratio between the maximum tensile and shear stress intensity factors (SIFs) was proposed by our group to successfully predict both Mode I and Mode II fracture under arbitrary loading conditions [31]. It has been applied for TM [32] and THM [16] coupling conditions and needs to be further developed for THMC coupling case.

In this work, THMC coupling indicator was defined based on rock porosity for representing the influencing degree of THMC coupling fields on stress field, which can be continuously determined by a novel real-time measurement method of permeability (related to porosity). A new fracture criterion was proposed to predict Mode I or Mode II fracture (including crack initiation load and angle, and fracture mode) for brittle rock under THMC coupling condition. Self-designed THMC coupling tests and scanning electron microscope tests were conducted on pre-cracked red sandstone specimens for verifying the effectiveness of the newly established THMC coupling fracture criterion.

## 2 THMC coupling indicator

### 2.1 Definition of THMC coupling indicator

For brittle rock, the interaction effect among temperature, seepage, stress and chemical (i.e., THMC) fields is mainly manifested as follows: (1) the temperature field has effect on density and viscosity of fluid, mechanical properties of rock, and chemical reaction rate and equilibrium; (2) the seepage field causes heat convection and conduction, rock deformation, and mineral dissolution and precipitation; (3) the stress field not only induces heat energy by relative friction, but also changes rock permeability, and transmission and diffusion paths of chemical solution; (4) the chemical field generates heat absorption or release, influences water permeability and conductivity by changing chemical composition and structural characteristics of rock, and mechanical property. And eventually, the coupled effect of THMC fields on rock can be reflected by changing the microstructure parameters of rock (i.e., rock porosity) [33]. Thus, the rock porosity acts as a

suitable relevant parameter to represent the coupled effect of THMC fields.

Under THMC coupling condition, the rock porosity would be changed from its initial value ( $n_0$ ) to arbitrary value ( $n$ ), which leads to the changes of effective normal and shear stresses. Based on rock porosity, a THMC coupling indicator ( $\lambda_n$ ) can be defined in the following form:

$$\lambda_n = \frac{n - n_0}{1 - n_0} \quad (1)$$

When  $n=n_0$  (initial state),  $\lambda_n=0$  (without THMC coupling effect on stress field) and when  $n \rightarrow 1$  (tends to failure),  $\lambda_n \rightarrow 1$  (with the largest THMC coupling effect on stress field). It is seen that the THMC coupling indicator  $\lambda_n$  in terms of the porosity ( $n$ ) can represent the influencing degree of THMC coupling field on stress field and has a clear physical meaning. In addition, it can be determined continuously during the THMC coupling test based on a novel real-time measurement method of permeability.

**2.2 Determination of THMC coupling indicator**

Based on the definition of THMC coupling indicator  $\lambda_n$  in Eq. (1), the key to determine  $\lambda_n$  is to measure rock porosity  $n$ . However, it is extremely difficult to monitor the rock porosity during test (especially for tri-axial compression test). By considering that the porosity of such rock material has significance effect on its permeability,  $\lambda_n$  may be determined indirectly by measuring the permeability [34,35].

(1) Novel real-time measurement method of

permeability

Figure 1 shows the schematic diagram of material testing system (MTS) 815, including temperature loading system (T), hydraulic pressure loading system (H), and axial pressure and confining pressure loading systems (M), where the hydraulic pressure is applied on the rock specimen by controlling the displacement of the piston.

During the test, keep water outlet open for making the water pass through rock specimen. Under THMC coupling condition, as the axial pressure is increased, the displacement of the hydraulic pressure piston is changed for keeping hydraulic pressure stable. Thus, the permeability of rock can be determined by the displacement of the hydraulic pressure piston recorded by the computer automatically.

During the test, water flow  $Q$  ( $m^3/s$ ) passing through specimen can be obtained by the displacement of hydraulic pressure piston  $s$  (m) as follows:

$$Q = \frac{A_0(s_2 - s_1)}{t_2 - t_1} = A_0 \cdot \frac{ds}{dt} \quad (2)$$

where  $A_0$  ( $m^2$ ) is cross-sectional area of the hydraulic pressure piston related to testing machine ( $A_0=0.004 m^2$ );  $ds/dt$  (m/s) can be recorded automatically by the testing machine.

According to Darcy law, permeability coefficient  $k_0$  (m/s) can be expressed as

$$k_0 = \frac{Ql}{A\Delta h} \quad (3)$$

where  $A$  ( $m^2$ ) and  $l$  (m) are cross-sectional area and the height of the specimen, respectively,  $\Delta h$  (m) is

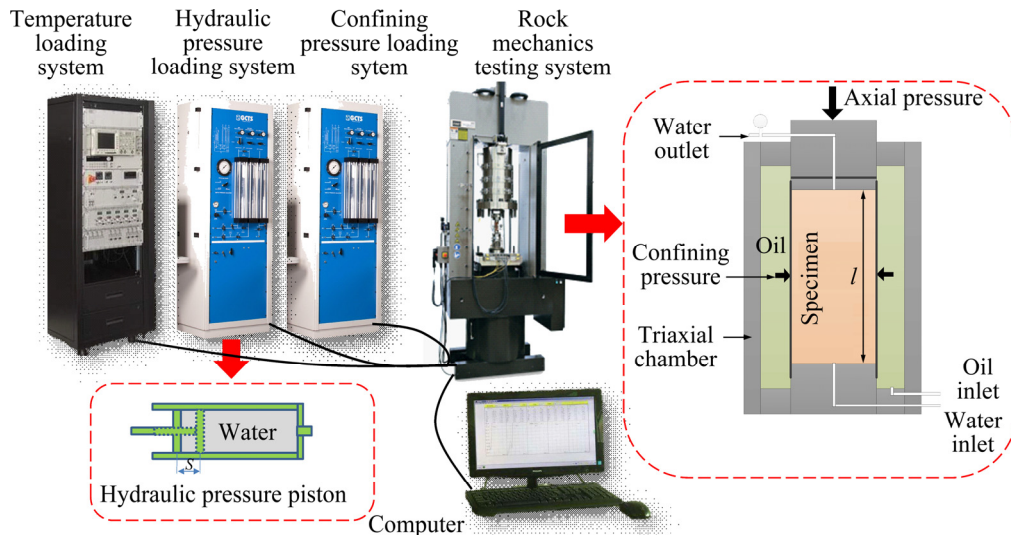


**Fig. 1** Schematic diagram of material test system (MTS) 815

pressure-head of the specimen, which is related to hydraulic pressure.

The relationship between permeability  $k$  ( $\text{m}^2$ ) and permeability coefficient  $k_0$  is

$$k_0 = k \frac{\rho g}{\mu} \quad (4)$$

So, the permeability of rock can be obtained by

$$k = \frac{\mu A_0 l}{\rho g A \Delta h} \cdot \frac{ds}{dt} \quad (5)$$

where  $\rho$  ( $\text{kg}/\text{m}^3$ ) and  $\mu$  ( $\text{Pa}\cdot\text{s}$ ) are the density and viscosity of water ( $\mu=1.001\times 10^{-3}$   $\text{Pa}\cdot\text{s}$  at room temperature), respectively;  $g(=9.8$   $\text{m}/\text{s}^2$ ) is the acceleration of gravity.

## (2) Measurement of permeability

Red sandstone adopted in the tests is from Yunnan province in China and has a good macroscopic homogeneity. According to X-ray diffraction test, its main mineral composition is as follows: quartz (69.1%), feldspar (13.4%), calcite (6.2%) and dolomite (3.6%). Four cylindrical specimens of red sandstone ( $d50$   $\text{mm} \times 100$   $\text{mm}$ ) were prepared, named sequentially from S1 to S4 (Fig. 2). Table 1 lists their porosities measured by ISRM (International Society for Rock Mechanics) suggested testing methods [36].



**Fig. 2** Red sandstone cylinder specimens in permeability test

**Table 1** Porosities measured by ISRM, and test results of permeability by our method and transient pressure method

Sample	$n/\%$	$k/\text{m}^2$	
		This method	Transient pressure method
S1	2.83	$1.33 \times 10^{-16}$	$1.37 \times 10^{-16}$
S2	3.24	$1.83 \times 10^{-16}$	$1.69 \times 10^{-16}$
S3	4.08	$2.50 \times 10^{-16}$	$2.61 \times 10^{-16}$
S4	4.51	$3.29 \times 10^{-16}$	$3.09 \times 10^{-16}$

The newly proposed method was adopted to determine their permeability with MTS 815 (Fig. 1). Before the test, specimen needs to be tightly sealed with heat-shrinkable hose for preventing mixing water with oil. The hydraulic pressures at the top and bottom of specimen are 0 and 2.5 MPa, respectively, and the confining pressure is 3 MPa. In addition, it needs to be noted that water outlet is open for ensuring the water to pass through rock specimen. After the test, the displacement of hydraulic pressure piston varying with time would be stored by the computer automatically.

For proving the reliability of the newly proposed method, transient pressure method [37] was used to remeasure the permeability. The hydraulic pressures and confining pressure have the same values as those in the new method. The water outlet is closed in order to make hydraulic pressure at the specimen bottom gradually decay to zero. The computer would record the variation of hydraulic pressure with time.

Figure 3 shows the displacement of hydraulic pressure piston–time curve and hydraulic pressure–time curve for different rock specimens. It can be seen that for all of specimens, the displacement of hydraulic pressure piston is increased linearly (i.e.,  $ds/dt$  is constant) with the increase of time (our method). This is because the hydraulic pressures at the top and the bottom of specimen are 0 and 2.5 MPa, respectively, and they are always fixed. However, the hydraulic pressure is decreased nonlinearly as the time changes (transient pressure method), which results from the fixed displacement of hydraulic pressure piston.

In our method, the permeability of red sandstone specimen can be readily calculated by substituting the test result ( $ds/dt$ ) into Eq. (5). In the transient pressure method, the permeability of the specimen can be determined by

$$k = \mu \zeta V \ln\left(\frac{P_1}{P_2}\right) / [2\Delta t \left(\frac{A}{l}\right)] \quad (6)$$

where  $V$  is reference volume ( $V=3.32 \times 10^{-4}$   $\text{m}^3$ );  $\zeta$  is the compressibility of water ( $\zeta=453 \times 10^{-12}$   $\text{Pa}^{-1}$ );  $P_1$  and  $P_2$  are hydraulic pressures of the specimen bottom at  $t_1$  and  $t_2$ , respectively;  $\Delta t=t_1-t_2$ , and  $\Delta t$  is usually chosen in middle section (Points  $M$ ,  $N$  in Fig. 3(a)) of hydraulic pressure–time curve.

Table 1 lists the permeability of red sandstone specimens obtained by our method and transient

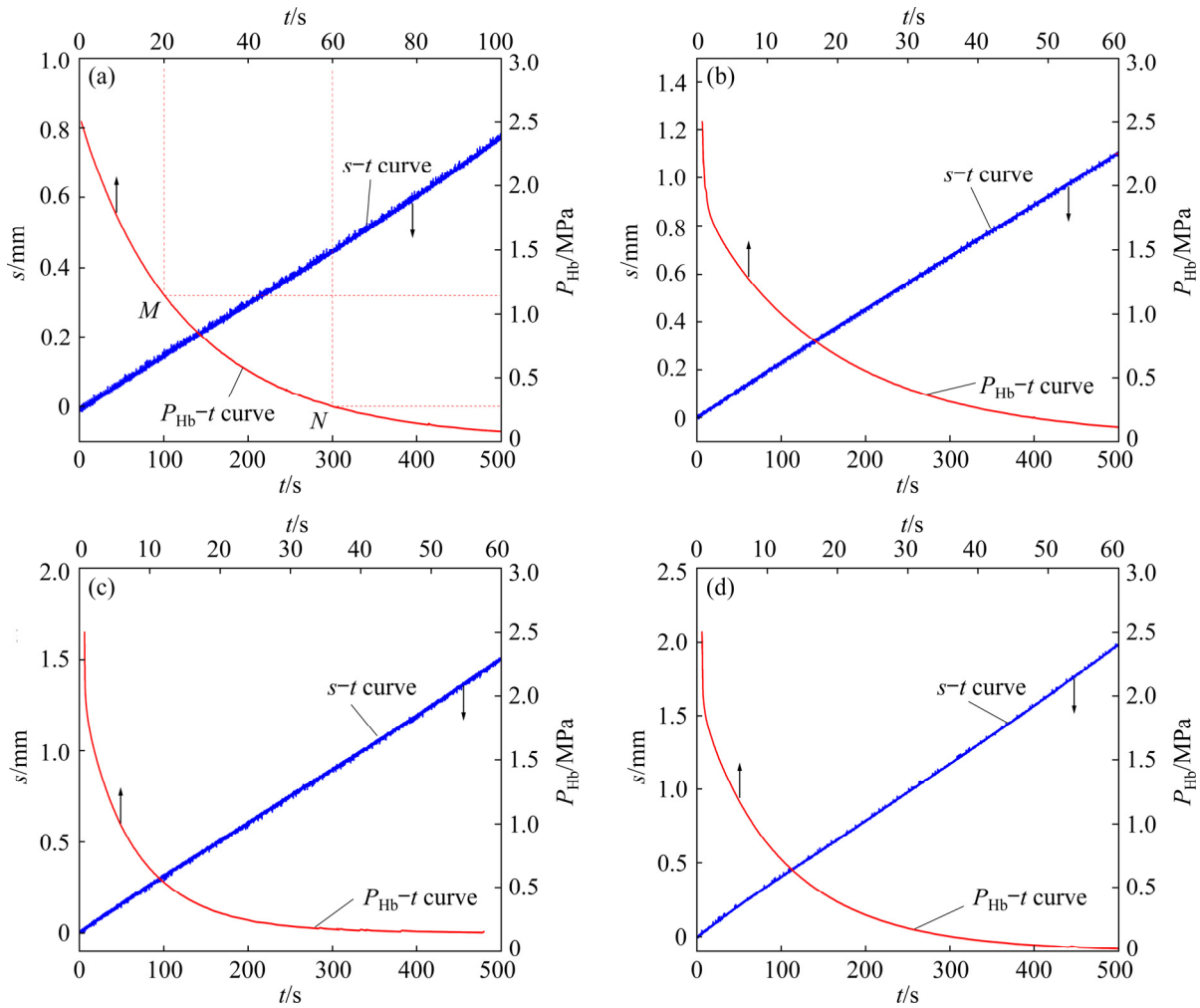


**Fig. 3** Displacement of hydraulic pressure piston–time curve and hydraulic pressure ( $P_{Hb}$ )–time curve for different red sandstone samples: (a) S1; (b) S2; (c) S3; (d) S4

pressure method. It is seen that our results agree quite well with those obtained by the transient pressure method, which can prove the reliability of our method.

(3) Relationship between porosity and permeability

With the help of fitting method [38], the relationship between porosity and permeability can be obtained by

$$\lg n = 7 + 0.5377 \lg k, R^2 = 0.993 \quad (7)$$

Under THMC coupling condition, the indicator  $\lambda_n$  can be determined by substituting Eq. (7) into Eq. (1).

It needs to be noted that although there are many methods available to measure the permeability of rock material, such as transient pressure method, pressure–attenuation method [39] and pulse–decay method [40,41], these methods are

limited to rock specimen under constant loading condition or natural state and unsuitable for quasi-static loading condition (where axial pressure is changed). Comparatively, the new real-time measurement method of permeability has advantage of wider application over transient pressure method, pressure–attenuation method and pulse–decay method, since it can be applied to continuously measuring the permeability under quasi-static loading condition as well as THMC coupling condition.

### 3 THMC coupling fracture criterion

#### 3.1 Calculation model

Figure 4 presents a standard cylinder specimen of rock ( $d50 \text{ mm} \times 100 \text{ mm}$ ) containing an oriented penetrating crack ( $2a=30 \text{ mm}$ ,  $\theta=45^\circ$ , and  $t=2 \text{ mm}$ )

under a specific temperature  $T$ , hydraulic pressure  $P_H$  (applied on the crack surface), confining pressure  $P_M$ , axial pressure  $P_L$  and chemical solution pH, i.e., THMC coupling condition. The rectangular coordinate system  $(xoy)$  and polar coordinate system  $(o_1r_1)$  are set at the crack center  $o$  and at the crack tip  $o_1$ , respectively.

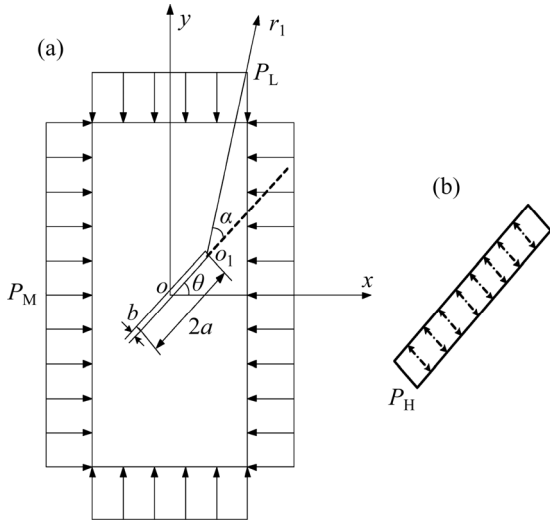


Fig. 4 Pre-cracked cylinder specimen under THMC coupling condition: (a) Front view; (b) Enlarged crack

### 3.2 Fracture criterion

By considering the effect of THMC coupling indicator  $\lambda_n$  on stress field, the effective normal ( $\sigma_{THMC}(\theta)$ ) and shear ( $\tau_{THMC}(\theta)$ ) stresses on the original crack surface are expressed as

$$\begin{cases} \sigma_{THMC}(\theta) = \frac{1}{1-\lambda_n} \left( \frac{P_L + P_M}{2} \right) + \\ \frac{1}{1-\lambda_n} \left[ \frac{P_L - P_M}{2} \cos(2\theta) + P_H \right] \\ \tau_{THMC}(\theta) = \frac{P_L - P_M}{2(1-\lambda_n)} \sin(2\theta) \end{cases} \quad (8)$$

where compressive stress is defined to be positive.

The Mode I and Mode II ( $K_I^{\lambda_n}(\theta)$ ,  $K_{II}^{\lambda_n}(\theta)$ ) SIFs at the original crack tip become

$$\begin{cases} K_I^{\lambda_n}(\theta) = \sigma_{THMC}(\theta)\sqrt{\pi a} = \left[ \frac{P_L + P_M}{2(1-\lambda_n)} \right] \sqrt{\pi a} + \\ \left[ \frac{P_L - P_M}{2(1-\lambda_n)} \cos(2\theta) + P_H \right] \sqrt{\pi a} \\ K_{II}^{\lambda_n}(\theta) = \tau_{THMC}(\theta)\sqrt{\pi a} = \left[ \frac{P_L - P_M}{2(1-\lambda_n)} \sin(2\theta) \right] \sqrt{\pi a} \end{cases} \quad (9)$$

Under THMC coupling condition, the original crack would be initiated and then propagated at an arbitrary angle of  $\alpha$ , where the normal and shear stress components are

$$\begin{cases} \sigma_\alpha = \frac{1}{2\sqrt{2\pi r}} \cos \frac{\alpha}{2} [K_I^{\lambda_n}(\theta)(1 + \cos \alpha)] - \\ \frac{1}{2\sqrt{2\pi r}} \cos \frac{\alpha}{2} [3K_{II}^{\lambda_n}(\theta) \sin \alpha] \\ \tau_\alpha = \frac{1}{2\sqrt{2\pi r}} \cos \frac{\alpha}{2} [K_I^{\lambda_n}(\theta) \sin \alpha] + \\ \frac{1}{2\sqrt{2\pi r}} \cos \frac{\alpha}{2} [K_{II}^{\lambda_n}(\theta) \sin \alpha (3 \cos \alpha - 1)] \end{cases} \quad (10)$$

The definitions of Mode I and Mode II ( $K_I^{\lambda_n}(\alpha)$ ,  $K_{II}^{\lambda_n}(\alpha)$ ) SIFs at a angle of  $\alpha$  with respect to the original crack are

$$\begin{cases} K_I^{\lambda_n}(\alpha) = \lim_{r \rightarrow 0} (\sigma_\alpha \sqrt{2\pi r}) \\ K_{II}^{\lambda_n}(\alpha) = \lim_{r \rightarrow 0} (\tau_\alpha \sqrt{2\pi r}) \end{cases} \quad (11)$$

So, there are

$$\begin{cases} K_I^{\lambda_n}(\alpha) = \frac{1}{2} \cos \frac{\alpha}{2} [K_I^{\lambda_n}(\theta)(1 + \cos \alpha)] - \\ \frac{1}{2} \cos \frac{\alpha}{2} [3K_{II}^{\lambda_n}(\theta) \sin \alpha] \\ K_{II}^{\lambda_n}(\alpha) = \frac{1}{2} \cos \frac{\alpha}{2} [K_I^{\lambda_n}(\theta) \sin \alpha] + \\ \frac{1}{2} \cos \frac{\alpha}{2} [K_{II}^{\lambda_n}(\theta) \sin \alpha (3 \cos \alpha - 1)] \end{cases} \quad (12)$$

Based on the fracture criterion of maximum tensile and shear SIF ratio proposed by our research group [31], a new THMC coupling fracture criterion can be established as follows:

$$\begin{cases} \frac{K_{II\alpha\max}^{\lambda_n}}{K_{I\alpha\max}^{\lambda_n}} < \frac{K_{IIC}}{K_{IC}} \quad (\text{Mode I fracture}) \\ K_{I\alpha\max}^{\lambda_n} = K_{IC} \\ \frac{K_{II\alpha\max}^{\lambda_n}}{K_{I\alpha\max}^{\lambda_n}} > \frac{K_{IIC}}{K_{IC}} \quad (\text{Mode II fracture}) \\ K_{II\alpha\max}^{\lambda_n} = K_{IIC} \end{cases} \quad (13)$$

Therefore, Mode I or Mode II crack initiation load ( $P_{LIC}$  or  $P_{LIIC}$ ) and angle (a positive angle of  $\alpha_{IC}$  or a negative angle of  $\alpha_{IIC}$ ) can be calculated by

$$\left\{ \begin{array}{l} \frac{\partial K_I^{\lambda_n}(\alpha)}{\partial \alpha} = 0, \frac{\partial^2 K_I^{\lambda_n}(\alpha)}{\partial \alpha^2} < 0 \Rightarrow \begin{cases} P_{LIC} \\ \alpha_{IC} \end{cases} \\ K_I^{\lambda_n}(\alpha)_{\max} = K_{IC} \end{array} \right. \quad \text{(Mode I fracture)}$$

or

$$\left\{ \begin{array}{l} \frac{\partial K_{II}^{\lambda_n}(\alpha)}{\partial \alpha} = 0, \frac{\partial^2 K_{II}^{\lambda_n}(\alpha)}{\partial \alpha^2} < 0 \Rightarrow \begin{cases} P_{LIIC} \\ \alpha_{IIIC} \end{cases} \\ K_{II}^{\lambda_n}(\alpha)_{\max} = K_{IIIC} \end{array} \right. \quad \text{(Mode II fracture)}$$

(14)

Whether Mode I or Mode II fracture takes precedence to occur at crack initiation angle  $\alpha_{IC}$  or  $\alpha_{IIIC}$  depends on whether the crack initiation load  $P_{LIC}$  or  $P_{LIIC}$  is smaller, i.e.,

$$\left\{ \begin{array}{l} P_{LIC} < P_{LIIC} \Rightarrow \begin{cases} P_C = P_{LIC} \\ \alpha_C = \alpha_{IC} \end{cases} \quad \text{(Mode I fracture)} \\ P_{LIC} > P_{LIIC} \Rightarrow \begin{cases} P_C = P_{LIIC} \\ \alpha_C = \alpha_{IIIC} \end{cases} \quad \text{(Mode II fracture)} \end{array} \right. \quad \text{or} \quad (15)$$

It is found that from the newly established fracture criterion, the crack initiation parameters (crack initiation angle and loads, and fracture mode) under THMC coupling condition can be calculated by the crack sizes ( $a$ ,  $\theta$ ), external loading ( $P_H$ ,  $P_M$ ), fracture toughness ( $K_{IC}$  and  $K_{IIIC}$ ) and THMC coupling indicator ( $\lambda_n$ ). Furthermore, although rock specimen containing single crack is taken into account in the calculation model, this fracture criterion can be also applied to studying multiple cracks and multiple crack–hole problems under THMC coupling condition based on the interacting SIF at each crack-tip derived from our previous work [42].

### 4 Test verification

#### 4.1 Test arrangements

Rock material is the same as that in the permeability test. Figure 5 shows a cylindrical red sandstone ( $d50 \text{ mm} \times 100 \text{ mm}$ ) containing an oriented penetrating crack ( $2a=30 \text{ mm}$ ,  $\theta=45^\circ$ , and  $b=2 \text{ mm}$ ). In order to apply the hydraulic pressure ( $P_H$ ) on the surface of the oriented crack, a small vertical hole ( $d3 \text{ mm} \times 50 \text{ mm}$ ) is drilled from the center of the specimen bottom to the oriented

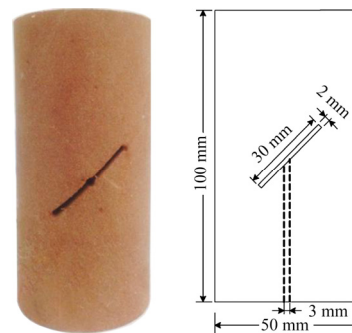
crack surface.

Table 2 lists the main mechanical parameters of rock specimen at room temperature. In this study, three-point bending test and shear-box test were employed to determine Mode I and Mode II fracture toughness. As shown in Fig. 6, rock specimens were square beams with size of  $250 \text{ mm} \times 50 \text{ mm} \times 50 \text{ mm}$  in three-point bending test and  $50 \text{ mm} \times 50 \text{ mm} \times 50 \text{ mm}$  in shear-box test, respectively. A penetrating crack with length of  $25 \text{ mm}$  was prefabricated in rock specimen. The fracture toughness of Mode I and Mode II can be readily determined by the crack initiation loads obtained from load–displacement curves ( $K_{IC}=0.60 \text{ MPa} \cdot \text{m}^{0.5}$ , and  $K_{IIIC}=1.21 \text{ MPa} \cdot \text{m}^{0.5}$ ).

As shown in Fig. 1, MTS815 was used to determine the crack initiation load and angle of red

**Table 2** Main mechanical parameters of red sandstone

$\sigma_t/\text{MPa}$	$\sigma_c/\text{MPa}$	$E/\text{GPa}$	$\nu$	$c/\text{MPa}$	$\phi/(^\circ)$
6.12	56.1	11.21	0.29	13.7	32



**Fig. 5** Cylinder specimen of red sandstone with inclined penetrating crack

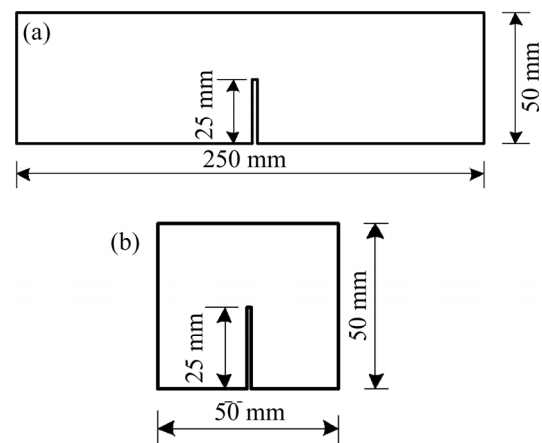


**Fig. 6** Sketch of three-point-bend (a) and shear-box (b) specimens

sandstone specimens under THMC coupling condition. Since the main purpose of the test is to verify the newly established fracture criterion, only three sets of tests are performed (Table 3). For current testing condition, it is hard to realize the true THMC coupling loads since the chemical solution would corrode tri-axial chamber of MTS 815. Thus, the specimens were immersed in a specific solution of  $T=20\text{ }^{\circ}\text{C}$  and  $\text{pH}=2$  for 120 h until pH value keeps relatively stable, and then loaded under different hydraulic pressures ( $P_H=2, 5\text{ MPa}$ ) and confining pressures ( $P_M=3, 6\text{ MPa}$ ), where  $P_M < 8\text{ MPa}$  for avoiding penetration of the isolation film wrapped on the pre-cracked specimen and  $P_H < P_M$  in order to avoid mixing oil and water. The oil (applying the confining pressure) is heated to a fixed temperature ( $T=20\text{ }^{\circ}\text{C}$ ) by the temperature loading system. The axial pressure is applied to the specimen at a constant displacement control rate ( $0.1\text{ mm/min}$ ) until rock failure. During the test, the axial pressure varying with time and hydraulic pressure varying with time are automatically recorded by the computer.

**Table 3** THMC coupling conditions for pre-cracked rock specimens

Specimen	$T/^{\circ}\text{C}$	$P_H/\text{MPa}$	$P_M/\text{MPa}$	pH
A1	20	2	6	2
A2	20	5	6	2
A3	20	2	3	2

As shown in Fig. 7, JSM-6360LV scanning electron microscope (SEM) was adopted to investigate the microscopic fracture characteristics of red sandstone specimens tested to ultimate failure. The SEM test was carried out on the small block with  $5\text{ mm} \times 5\text{ mm} \times 4\text{ mm}$  near the crack tip



**Fig. 7** JSM-6360LV scanning electron microscope

region of the fracture surface of the specimen. Before the test, the small block was dried in high temperature furnace and then sprayed with gold powder, since red sandstone has high porosity and moisture content, and low electric conductivity.

**4.2 Result and analysis**

**4.2.1 Axial stress and displacement of hydraulic pressure piston–time curves**

Figure 8 shows the curves of axial stress

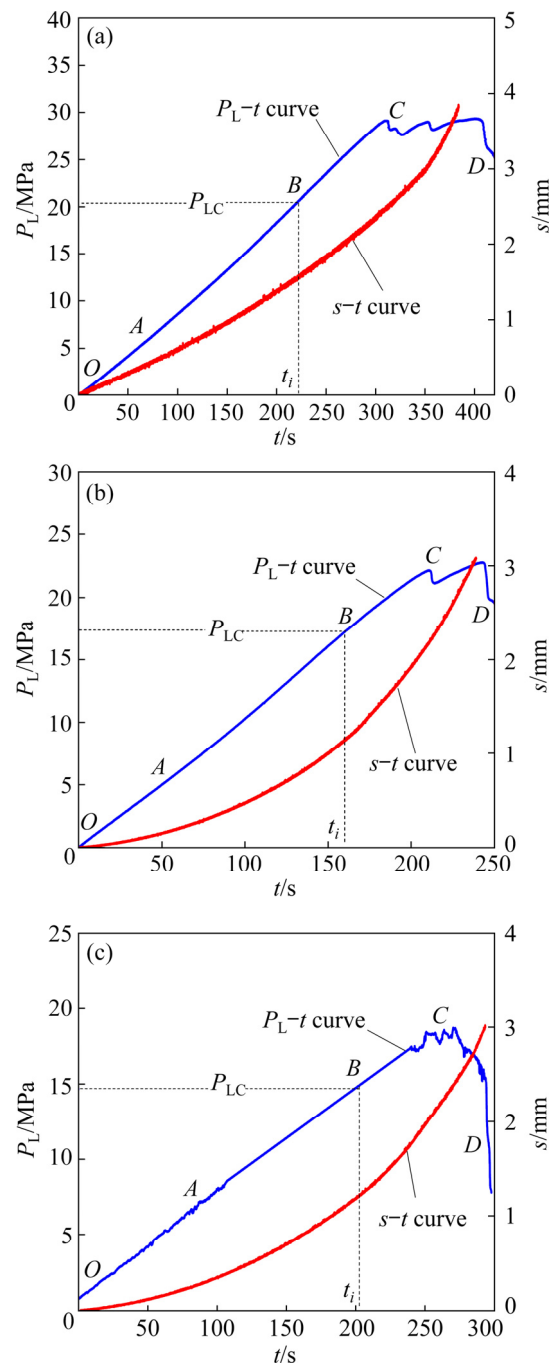


**Fig. 8** Axial pressure–time curves and displacement of hydraulic pressure piston–time curves under different THMC coupling conditions: (a) A1; (b) A2; (c) A3

varying with time ( $P_L-t$ ) and displacement of hydraulic pressure piston varying with time ( $s-t$ ) on pre-cracked red sandstone specimens under different THMC coupling conditions. All of  $P_L-t$  and  $s-t$  curves are mainly composed of four stages, i.e., micro-pore compaction ( $OA$ ), elastic deformation ( $AB$ ), crack propagation ( $BC$ ) and failure ( $CD$ ). In the stage of the micro-pore compaction, the  $P_L-t$  curves are concave downward and the slopes of  $s-t$  curves are increased gradually, since the initial pores are close rapidly with the increasing of axial stress. In the stage of the elastic deformation, the slopes of  $P_L-t$  and  $s-t$  curves keep relatively stable in spite of some irrecoverable processes (i.e., few micropore closure and microcrack initiation). In the stage of the crack propagation, the maximum SIFs at two tips of the original crack reach the fracture toughness of red sandstone and cracks initiate and propagate, which results in the upward concave  $P_L-t$  curves and downward concave  $s-t$  curves. In this stage, the axial stress at the original point  $B$  of upward concave  $P_L-t$  curves is crack initiation load  $P_{LC}$ , and accordingly, the crack initiation porosity ( $n_i$ ) can be calculated by substituting the slope of  $s-t$  curves at point  $B$  into the fitting result of  $n-k$  in Eq. (15). In the stage of the failure, the  $P_L-t$  curves present a rapid drop and the  $s-t$  curves have a rapid increase due to the coalescence of the original crack.

#### 4.2.2 Macroscopic fracture mechanism

Figure 9 shows fracture trajectories of pre-cracked red sandstone specimens under different THMC coupling conditions. It can be seen from Fig. 9 that, there exist two types of fracture trajectories: (1) The original crack initiates simultaneously from two crack tips along the approximately vertical direction to the original crack, and then gradually propagates along the direction of the axial stress (Specimens A2, A3), which corresponds to longitudinal fracture; (2) the original crack initiates simultaneously from two crack tips along another approximately vertical direction to the original crack, and then gradually departs towards the direction of the axial stress (Specimen A1), which corresponds to transverse fracture. In addition, as the hydraulic pressure is increased or the confining pressure is decreased, the fracture trajectory is changed from transverse fracture to longitudinal fracture.

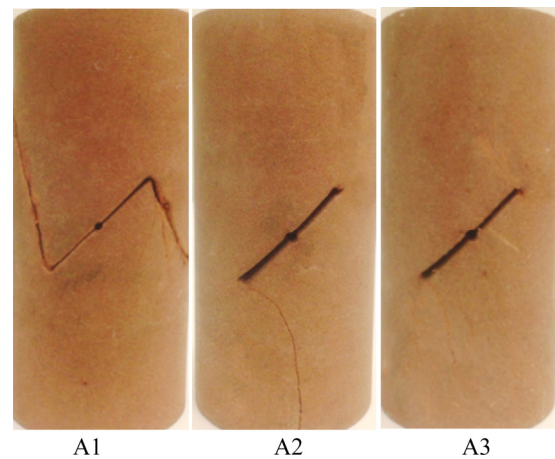


**Fig. 9** Fracture trajectories of pre-cracked red sandstone specimens under different THMC coupling conditions

#### 4.2.3 Microscopic fracture mechanism

Figure 10 presents the SEM morphologies of fracture surface near crack tip region of specimens under different THMC coupling conditions. It is observed that for Specimen A1, the most outstanding feature is that the fracture surface has many distributed slip-steps and fish-scale patterns, which is mainly caused by the transgranular fracture. There are fine and dense streamline patterns on the cleavage plane. This means that a large amount of energy needs to be dissipated when the original crack is initiated. These SEM morphologies of fracture surface indicate that principal microscopic characteristic is shearing (Mode II) fracture for the crack initiation of Specimen A1. Specimens A2 and A3 have similar SEM fracture morphologies, different from Specimen A1. Their fracture surfaces have a number of crystal particles in the shapes of rock block and rock sugar, which is mainly caused by the intergranular fracture. The streamline patterns on the cleavage plane of Specimens A2 and A3 is less than those of Specimen A1. This means that a low amount of energy is dissipated when the original crack is initiated, and the original crack for Specimens A2 and A3 is easier to initiate than that for Specimen A1. These SEM morphologies of fracture surface indicate that principal microscopic characteristic is tensile (Mode I) fracture for the crack initiation of Specimens A2 and A3.

#### 4.2.4 Comparison of test and prediction results

Table 4 lists the test and prediction results of crack initiation load and angle and fracture mode, where crack initiation parameters are calculated by

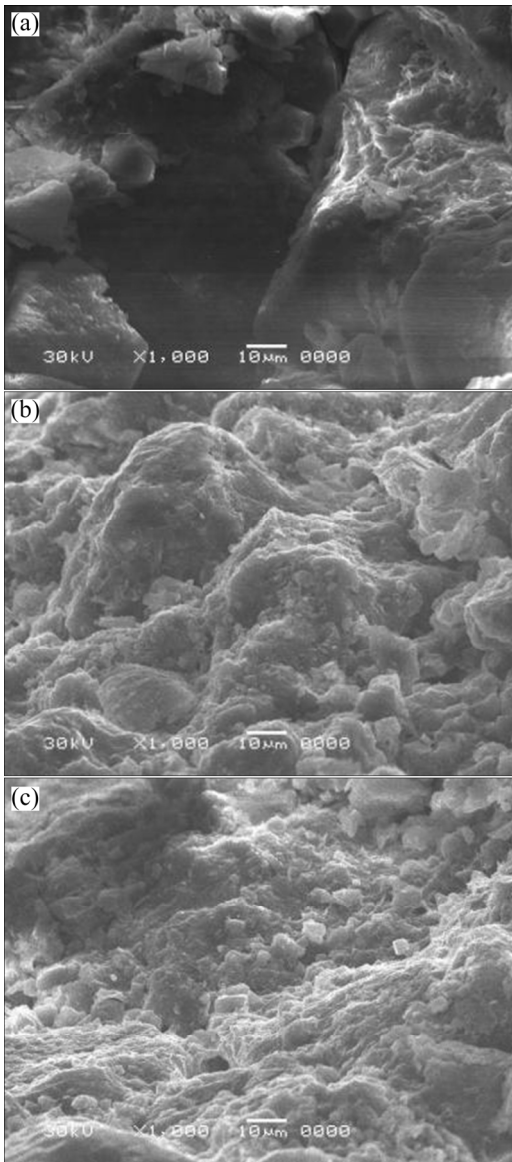


**Fig. 10** SEM fracture morphologies of fracture surfaces of specimens under different THMC coupling conditions: (a) A1; (b) A2; (c) A3

substituting the following four sets of parameters into Eqs. (7) and (8): (1) crack sizes ( $a$ ,  $\theta$ ); (2) loading conditions ( $P_H$ ,  $P_M$ ); (3) material properties

( $K_{IC}$  and  $K_{IIC}$  at 20 °C and pH 2); (4) THMC coupling indicator ( $\lambda_n$ , i.e.,  $n_0$  and  $n_i$ ). It is found that crack initiation load is decreased and the mode of fracture is changed from Mode II ( $\alpha_C < 0$ ) to Mode I ( $\alpha_C > 0$ ) as hydraulic pressure is increased, while the confining pressure has opposite effect. This is mainly because the hydraulic pressure would result in the open tendency of the crack and the increase of the Mode I SIFs at crack tips. However, the confining pressure usually causes the closing tendency of the crack, and indirectly decreases the Mode I SIFs at crack tips. Increasing or decreasing Mode I SIFs makes Mode I or Mode II fracture more likely to occur based on the newly proposed THMC coupling fracture criterion (Eq. (13)). For brittle rock, its fracture toughness of Mode II has larger values than that of the Mode I fracture toughness, which would lead to the specimen subjected to the Mode II fracture with a larger crack initiation load. It is also found that the test results of crack initiation load and angle and fracture mode agree well with the prediction results, which proves the effectiveness of the newly established THMC coupling fracture criterion.

In addition, the cylindrical sample is used in this test for easily measuring the THMC coupling factor. This is a typical 3D problem, while the newly established fracture criterion is based on two-dimensional model since it is very difficult to derive the analytical formula of SIFs for the pre-crack cylinder [43]. Therefore, finite element method is used to calculate the SIFs in pre-cracked cylinder and pre-cracked plate in previous literature [44]. It is found that they have almost the same values. Therefore, it is appropriate to use pre-cracked cylindrical specimen to verify the validity of the new fracture criterion under THMC coupling condition.

**Table 4** Test and prediction results of crack initiation load and angle, and fracture mode under different THMC coupling conditions

Specimen	$k_i/10^{-16}m^2$	$n_0/\%$	$n_i/\%$	Prediction results					Test results		
				$P_{LIC}/MPa$	$\alpha_{IC}/(^{\circ})$	$P_{LIIC}/MPa$	$\alpha_{IIC}/(^{\circ})$	Fracture mode	$P_{LC}/MPa$	$\alpha_C/(^{\circ})$	Fracture mode
A1	7.4	2.7	7.3	23.1	99.8	21.8	-108.6	II	20.7	-107.4	II
A2	10.4	3.8	8.8	17.4	96.6	18.3	-113.1	I	17.2	95.6	I
A3	8.9	4.1	8.1	15.1	93.2	17.7	-111.7	I	14.9	88.9	I

## 5 Conclusions

(1) A new THMC coupling fracture criterion is established to predict the crack initiation load and angle and fracture mode of brittle rock based on the proposed THMC coupling indicator (in terms of rock porosity) and fracture criterion of maximum tensile and shear SIF ratio. It has wider application than the common fracture criteria in predicting both Mode I and Mode II fracture under THMC coupling condition. It can be further extended to predict THMC coupling fracture of multi-crack problem.

(2) A novel real-time measurement method of permeability is proposed to continuously determine the THMC coupling indicator under THMC coupling condition, and can be verified by permeability test based on transient pressure method. The new method has advantage of continuously measuring permeability under quasi-static loading condition, over transient pressure method, pressure–attenuation method and pulse–decay method (only under constant loading condition).

(3) The self-designed THMC coupling tests and scanning electron microscope tests of pre-cracked red sandstone specimens show that increasing hydraulic pressure usually results in the decrease of the crack initiation load and the occurrence of Mode I fracture, while the confining pressure has opposite effect. The test results of crack initiation load and angle, and fracture mode agree well with the prediction ones, which can prove the effectiveness of the THMC coupling fracture criterion.

## Acknowledgments

The authors are grateful for the financial supports from the National Natural Science Foundation of China (Nos. 51474251, 51874351), and the Excellent Postdoctoral Innovative Talents Project of Hunan Province, China (No. 2020RC2001).

## References

[1] YUI M. A research program for numerical experiments on coupled thermo-hydro-mechanical and chemical processes [J]. *Nature*, 2002, 300(5894): 747–750.

- [2] ITO A, YUM M, SUGITA Y, KAWAKAMI S. A research program for numerical experiments on the coupled thermo-hydro-mechanical and chemical processes in the near-field of a high-level radioactive waste repository [J]. *Elsevier Geo-Engineering Book Series*, 2004, 2(4): 353–358.
- [3] TSANG C F. Introductory editorial to the special issue on the DECOVALEX-THMC project [J]. *Environmental Geology*, 2009, 57(6): 1217–1219.
- [4] ZHENG L, RUTQVIST J, XU H, BIRKHOFFER J T. Coupled THMC models for bentonite in an argillite repository for nuclear waste: Illitization and its effect on swelling stress under high temperature [J]. *Engineering Geology*, 2017, 30: 118–129.
- [5] PIOTR M, NIEDBALSKI Z. A comprehensive geomechanical method for the assessment of rockburst hazards in underground mining [J]. *International Journal of Mining and Science Technology*, 2020, 30(3): 345–355.
- [6] PARK C H, BOBET A. Crack initiation, propagation and coalescence from frictional flaws in uniaxial compression [J]. *Engineering Fracture Mechanics*, 2010, 77(14): 2727–2748.
- [7] YU S F, WU A X, WANG Y M. Insight into the structural evolution of porous and fractured media by forced aeration during heap leaching [J]. *International Journal of Mining and Science Technology*, 2018, 29(5): 803–807.
- [8] BRATOV V, KRIVTSOV A. Analysis of energy required for initiation of inclined crack under uniaxial compression and mixed loading [J]. *Engineering Fracture Mechanics*, 2019, 216: 1–7.
- [9] WONG L N Y, EINSTEIN H H. Systematic evaluation of cracking behavior in specimens containing single flaws under uniaxial compression [J]. *International Journal of Rock Mechanics and Mining Sciences*, 2009, 46(2): 239–249.
- [10] YANG S Q, JING H W. Strength failure and crack coalescence behavior of brittle sandstone samples containing a single fissure under uniaxial compression [J]. *International Journal of Fracture*, 2011, 168(2): 227–250.
- [11] YANG S Q. Fracture mechanical behavior of red sandstone containing a single fissure and two parallel fissures after exposure to different high-temperature treatments [M]. Springer Berlin Heidelberg, 2015.
- [12] FENG X T, CHEN S L, ZHOU H. Real-time computerized tomography (CT) experiments on sandstone damage evolution during triaxial compression with chemical corrosion [J]. *International Journal of Rock Mechanics and Mining Sciences*, 2004, 41(2): 181–192.
- [13] FENG X T, CHEN S L, LI S. Effects of water chemistry on microcracking and compressive strength of granite [J]. *International Journal of Rock Mechanics and Mining Sciences*, 2001, 38(4): 557–568.
- [14] LU Z D, CHEN C X, FENG X T, ZHANG Y L. Strength failure and crack coalescence behavior of sandstone containing single pre-cut fissure under coupled stress, fluid flow and changing chemical environment [J]. *Journal of Central South University*, 2014, 21(3): 1176–1183.
- [15] LI P, RAO Q H, MA W B, SU S L, MA C D. Coupled thermo-hydro-mechanical fractographic analysis of brittle

- rock [J]. *Chinese Journal of Rock Mechanics and Engineering*, 2014, 33(6): 1179–1186. (in Chinese)
- [16] LI P, RAO Q H, LI Z, JING J. Thermal-hydro-mechanical coupling stress intensity factor of brittle rock [J]. *Transactions of Nonferrous Metals Society of China*, 2014, 24(2): 499–508.
- [17] GALYON D S E, FAWAZ S A. Examination of the effects of specimen geometry on single edge-cracked tension specimens [J]. *Engineering Fracture Mechanics*, 2019, 209: 221–227.
- [18] ZONG Y J, HAN L J, MENG Q B, WANG Y C. Strength properties and evolution laws of cracked sandstone samples in re-loading tests [J]. *International Journal of Mining and Science Technology*, 2020, 30(2): 251–258.
- [19] SALIMI-MAJD D, SHAHABJ F, MOHAMMADI B. Effective local stress intensity factor criterion for prediction of crack growth trajectory under mixed mode fracture conditions [J]. *Theoretical and Applied Fracture Mechanics*, 2016, 85: 207–216.
- [20] ERDOGAN F, SIH G C. On the crack extension in plates under plane loading and transverse shear [J]. *Basic Engineering*, 1963, 85: 519–527.
- [21] MAITI S K, SMITH R A. Comparison of the criteria for mixed mode brittle fracture based on the preinstability of stress-strain field [J]. *International Journal of Fracture*, 1984, 24(1): 5–22.
- [22] CHANG K J. On the maximum strain criterion—A new approach to the angled crack problem [J]. *Engineering Fracture Mechanics*, 1981, 14(1): 107–124.
- [23] PALANISWAMY K, KNAUSS W G. Propagation of a crack under general in-plane tension [J]. *International Journal of Fracture*, 1972, 8(1): 114–117.
- [24] SIH G C. Strain energy–density factor applied to mixed mode crack problem [J]. *International Journal of Fracture*, 1974, 10(3): 305–321.
- [25] THEOCARIS P S, ANDRIANOPOULOS N P. The Mises elastic-plastic boundary as the core region in fracture criteria [J]. *Engineering Fracture Mechanics*, 1982, 16(3): 425–432.
- [26] YEHIA N A B. On the use of the T-criterion in fracture mechanics [J]. *Engineering Fracture Mechanics*, 1985, 22(2): 189–199.
- [27] LI X P, XIAO T L, DAI Y F. Coupling analysis of seepage and stress in jointed rock mass based on damage and fracture mechanics theory [C]//2011 International Conference on Electric Technology and Civil Engineering, ICETCE 2011-Proceedings. Lushan, China: IEEE, 2013: 6512–6516.
- [28] TAN L S, WANG S J. Analysis on mechanism and quantitative methods of chemical damage in water–rock interaction [J]. *Chinese Journal of Rock Mechanics and Engineering*, 2002, 21(3): 314–319. (in Chinese)
- [29] YI W, RAO Q H, LI Z, SHEN Q Q. A new measurement method of crack propagation rate for brittle rock under THMC coupling condition [J]. *Transactions of Nonferrous Metals Society of China*, 2019, 29(8): 1728–1736.
- [30] BAHMANI A, ALIHA M R M, SARBIJAN M J, MOUSAVI S S. An extended edge-notched disc bend (ENDB) specimen for mixed-mode I+II fracture assessments [J]. *International Journal of Solids and Structures*, 2020, 193: 239–250.
- [31] RAO Q H, SUN Z Q, STEPHANSSON O, LI C L, STILLBORG B. Shear fracture (Mode II) of brittle rock [J]. *International Journal of Rock Mechanics and Mining Sciences*, 2003, 40(3): 355–375.
- [32] WANG Z. Plane shear (Mode II) and anti-plane shear (Mode III) fracture theory and experiment analysis of rock at high temperature [D]. Changsha: Central South University, 2007. (in Chinese)
- [33] KOLDITZ O. Thermo-hydro-mechanical-chemical processes in fractured porous media: Modelling and benchmarking closed-form solutions [M]. Springer Berlin Heidelberg, 2012.
- [34] LIU H H, ZHENG L G, YANG J T. Relationships between permeability, porosity and effective stress for low-permeability sedimentary rock [J]. *International Journal of Rock Mechanics and Mining Sciences*, 2015, 78: 304–318.
- [35] PENG R, DI B, GLOVER P W J, WEI J, WU M. The effect of rock permeability and porosity on seismoelectric conversion: Experiment and analytical modelling [J]. *Geophysical Journal International*, 2019, 219: 328–345.
- [36] ISRM. Suggested methods for determining water content, porosity, density, absorption and related properties and swelling and slake-durability index properties. Part 2: Suggested methods for determining swelling and slake-durability index properties [J]. *International Journal of Rock Mechanics and Mining Sciences*, 1979, 16(2): 151–156.
- [37] WANG L, LIU J F, PEI J L, XU H N, BIAN Y. Mechanical and permeability characteristics of rock under hydro-mechanical coupling conditions [J]. *Environmental Earth Sciences*, 2015, 73(10): 5987–5996.
- [38] NEUMAIER A. Introduction to numerical analysis [M]. Cambridge University Press, 2001.
- [39] XUE H, EHLIG-ECONOMIDES C. Permeability estimation from fracture calibration test analysis in shale and tight gas [C]//Unconventional Resources Technology Conference. Denver, USA: Society of Petroleum Engineers, 2013: 12–14.
- [40] WANG Y, LIU S, ELSWORTH D. Laboratory investigations of gas flow behaviors in tight anthracite and evaluation of different pulse-decay methods on permeability estimation [J]. *International Journal of Coal Geology*, 2015, 149: 118–128.
- [41] FENG R, HARPALANI S, PANDEY R. Evaluation of various pulse-decay laboratory permeability measurement techniques for highly stressed coals [J]. *Rock Mechanics and Rock Engineering*, 2017, 50(2): 297–308.
- [42] YI W, RAO Q H, LUO S, SHEN Q Q, LI Z. A new integral equation method for calculating interacting stress intensity factor of multiple crack-hole problem [J]. *Theoretical and Applied Fracture Mechanics*, 2020, 102535. <https://doi.org/10.1016/j.tafmec.2020.102535>.
- [43] ANDERSON T L. Fracture mechanics: Fundamentals and applications [M]. CRC Press, 1991.
- [44] YI W. Combined effect of thermo-hydro-mechano-chemical multi-fields on fracture and cracking-resistance of brittle rock [D]. Changsha: Central South University, 2019. (in Chinese)

# 脆性岩石热-水-力-化学(THMC)耦合断裂准则

易 威, 饶秋华, 李 卓, 孙栋良, 沈晴晴

中南大学 土木工程学院, 长沙 410075

**摘 要:** 通过分析脆性岩石 THMC 耦合机理, 选取岩石孔隙率作为 THMC 耦合因子来表征 THMC 耦合场对应力场的影响。提出一种实时监测岩石渗透率(与孔隙率相关)的新型测试方法以确定 THMC 耦合因子。利用自行设计的 THMC 耦合试验和断口电镜扫描试验研究预制裂隙红砂岩宏观和微观断裂机理。结果表明: 水压越高, 围压越低, 起裂荷载越小, I 型断裂更易发生。理论预测结果与试验结果吻合较好, 验证新建立的 THMC 耦合断裂准则的有效性。该准则可进一步推广到研究 THMC 耦合下岩石多裂纹断裂机理。

**关键词:** THMC 耦合; 断裂准则; THMC 耦合因子; 脆性岩石

(Edited by Bing YANG)